A Portable Robotic Device for Autonomous Vascular Access

Haoyang Li[*1], Tenghui Xie[*1], Jinghai Pan[1], Yibo Zhao[1], Zhifan Yan[1], Jinyan Guo[1,3], Yu Chen[1], Junbo Ge[2], Peng Qi[1]

[*]Project Co-leads,

[1]Tongji University, [2]Fudan University, [3]Shanghai Tenth People's Hospital

Venipuncture is critical to a plethora of clinical interventions and is the most ubiquitous invasive routine in the U.S., with over 2.7 million procedures performed daily. The procedure is traditionally guided by visual inspection and palpation of the peripheral forearm veins. Once a suitable vein is located, a needle is then inserted into the center of the vessel. Oftentimes, however, it is difficult to estimate the depth of the vein or steer the needle if the vein moves or rolls. Poorly introduced needles may then result in complications such as increased pain, internal bleeding, or extravasation. The challenges of venipuncture are exacerbated in obese and dark-skinned patients where locating a vein can be difficult, as well as in pediatric and geriatric populations where the veins are often small and weak.

Unlike imaging-based methods, which rely on manual insertion, robotic strategies could altogether eliminate the dependence on practitioner experience and availability. Here, we present a portable venipuncture robot capable of steering needles and catheters into submilli-meter vessels with minimal supervision. The robot (Fig. 1 (a)), which offers 9-DOF, has a compact design consisting of a positioning unit (Fig. 1 (b)), a support unit (Fig. 1 (c)), an information processing unit (Fig. 1 (d)), a puncturing unit (Fig. 1 (e)) and a needle module (Fig. 1 (f)). As shown in Fig. 2, This robot uses a vascular localization technology that combines a NIR camera and an ultrasound device (st-1c transducer, frequency 7.5MHz, 48 lateral array elements, 80 axial array elements, element spacing 0.3mm) which is placed at the front of the robot. In the longitudinal section of blood vessels, ultrasonic images are used to perform vein segmentation and estimation of vein depth. The NIR optical imaging is used to segment the venous distribution in the horizontal direction.

Robotic System

The positioning unit, with its 4-DOF, consists of motor and ball screw drive modules. Three of them are translations along the x, y, and z axis, while the fourth is rotation along the z axis.

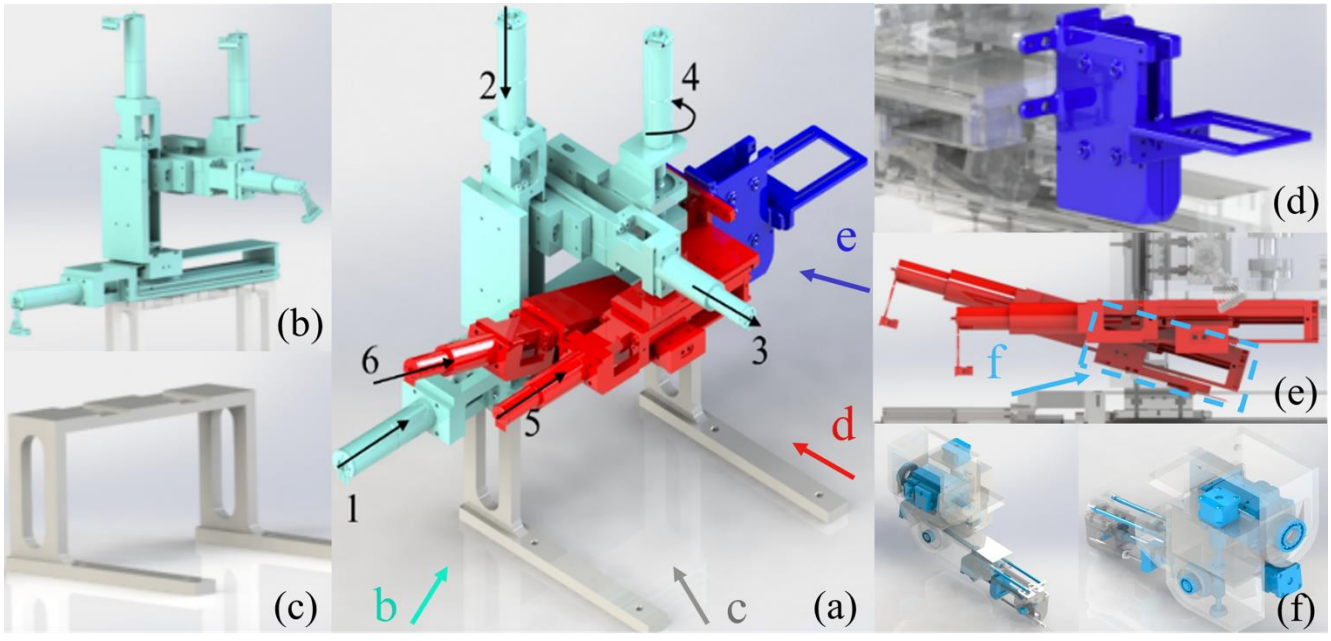

Fig. 1. An illustration of the Solidworks (CAD) model of the venipuncture robot, with the white color indicating the supporting unit, the blue color indicating the positioning unit, the red color indicating the puncturing unit, the purple color indicating the imaging unit, and the transparent color indicating the needle module.

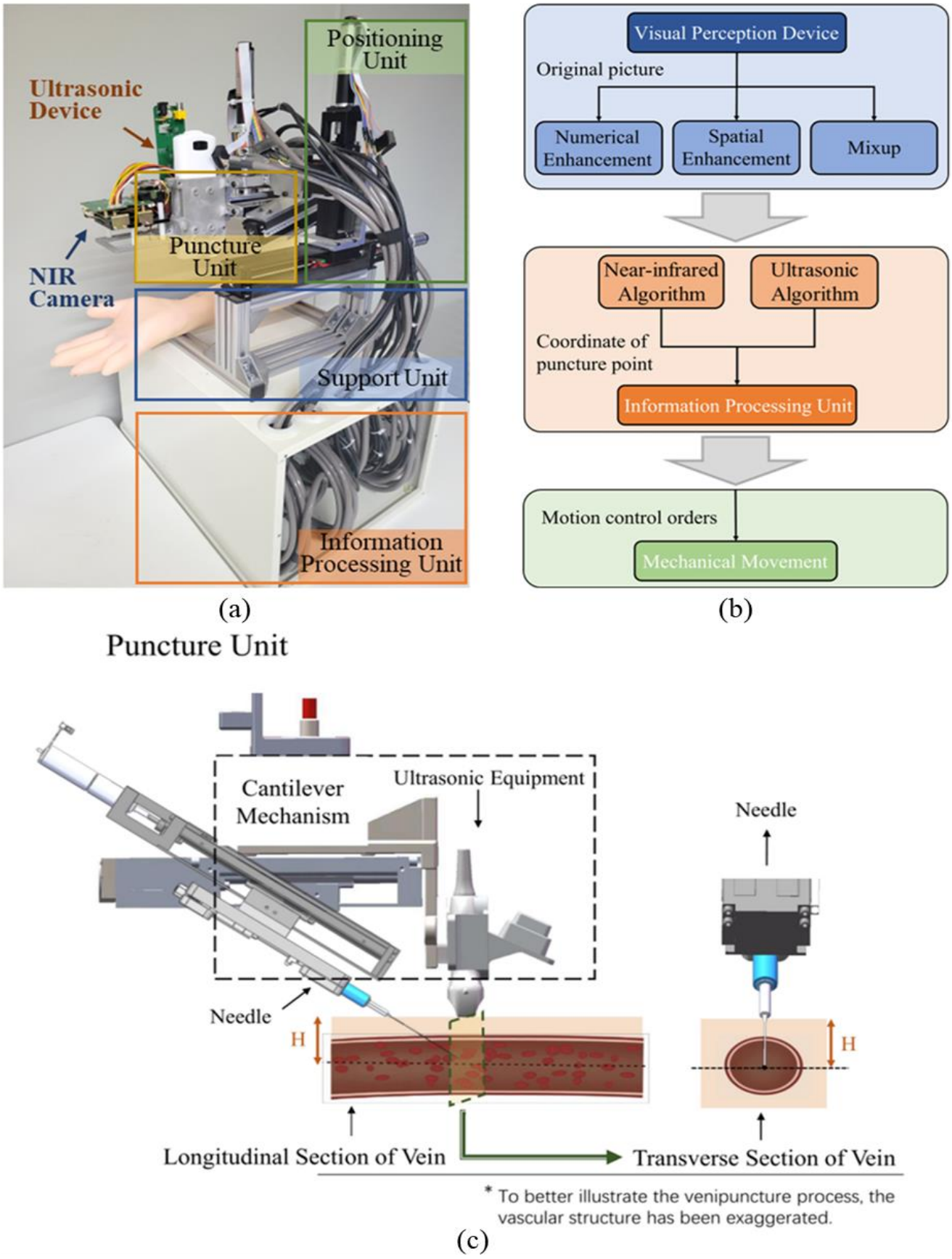

Fig. 2. An illustration of the venipuncture robot: (a) Mechatronics design of the robot; (b) Workflow of venipuncture; (c) Vascular localization based on ultrasound imaging, specifically in the longitudinal direction.

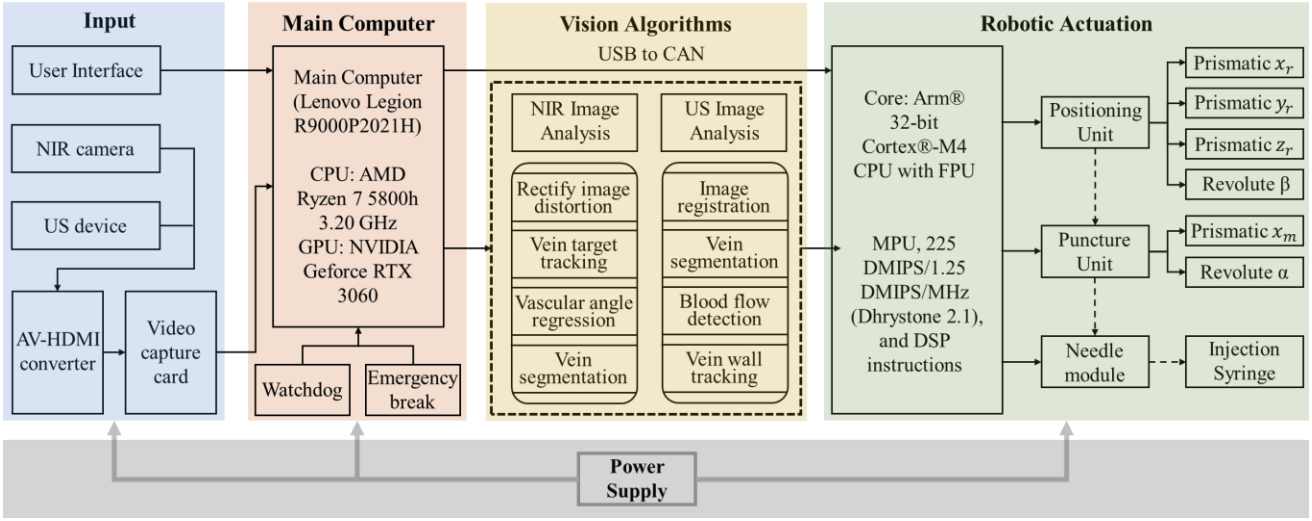

Fig. 3. Hardware and software system architecture design, depicting the process flow from image acquisition, signal processing, and robotic controls.

Motors 1, 2, and 3 operate jointly to move to the target x-y plane obtained by analyzing the NIR images using the NIR algorithm. The puncture angle is determined by motor 4. At the same time, the cantilever mechanism moves down as a whole to ensure that the ultrasonic equipment touches the skin correctly so that a clear ultrasound image can be collected and used for pre-puncture navigation. Upon contact with the skin, it can elicit high-quality longitudinal vein section images, the ultrasonic algorithm then calculates the depth of the puncture point. The puncturing unit has 2-DOF, is driven by a uni-axial mechanism, and can puncture under the guidance of an ultrasonic device. The movement of the needle along the y-direction is controlled by motor 5 in the puncturing unit, while motor 6 advances the needle module to the vein puncture point.

Mechanical Structure Design

Transmission part

The transmission part of the mechanical mechanism is a six-degree-of-freedom compact mechanism (Fig. 4(a)) designed with a reliable short transmission chain structure, which mostly consists of a precision ball screw and Maxon motor (Fig. 4(b)).

Low friction in ball screws yields high mechanical efficiency compared to alternatives. A typical ball screw may be 90 percent efficient, versus 20 to 25 percent efficiency of an Acme lead screw of equal size. Lack of sliding friction between the nut and screw lends itself to an extended lifespan of the screw assembly, reducing downtime for maintenance and parts replacement, while also decreasing demand for lubrication. In the meanwhile, the key features that set Maxon's electronically commutated EC motors apart are their excellent torque performance, high power, extremely wide speed range, and unrivaled service life. The outstanding controllability of the motors permits the creation of high-precision positioning drives.

Consequently thus, the transmission part with the advantages of high axial stiffness of ball screw, high transmission accuracy, high mechanical efficiency, etc., guarantee the positioning accuracy of Needle Module and the stability of puncture process.

3-DOF Needle Module

As shown in Fig. 5, the 3-DOF Needle Module consists of a linear stage driven by a lead screw spindle supported by ball sliders and a worm drive system.

The new kinematic geometry allows puncture needle the insertion angle to be controlled independently of the other DOF. A worm drive system (C in Fig. 5) is used to control the

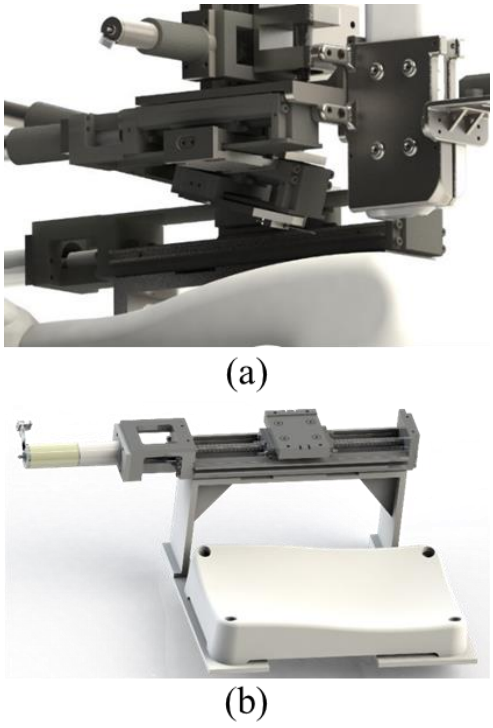

Fig. 4. An illustration of the transmission part of the venipuncture robot: (a) Transmission design of robot; (b) Precision ball screw and Maxon motor of the robot.

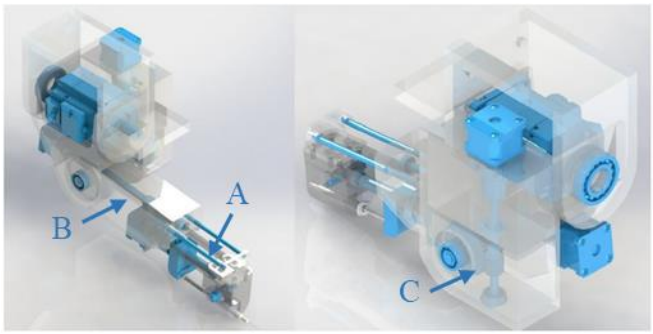

Fig. 5. Design of 3-DOF puncture needle manipulator with ball-screw drive and worm drive.

insertion angle to ensure self-locking of the rotational joint. This prevents free, unconstrained motion by the robot when electrical power is not being supplied to the system. This design is key to providing the needle to adjust the insertion angle to the optimal puncture angle without increasing the device size. Two ball screw mechanisms(A, and B in Fig. 5) are used to push the puncture needle into the blood vessel step by step according to the position specified by the control system. This design can accurately adjust the puncture speed of the needle during a puncture. This design also changes dramatically improves the puncture stability and needle tip positioning accuracy of the robot.

Mechanical Control Method

Coordinate Transformation

After obtaining the ultrasonic image of the target vein, the transformation between the image frame, the camera frame, and the world frame is needed to accurately map the puncture point coordinates in the image to the robot execution coordinates (Fig. 6). The relationship between the pixel unit coordinates of any point (u, v)in the image (Γ) and its corresponding millimeter unit coordinates (X, Y)satisfies the following homogeneous transformation matrix T.

$$\begin{bmatrix} u \\ v \\ l \end{bmatrix} = \begin{bmatrix} \frac{1}{dX} & 0 & u_0 \\ 0 & \frac{1}{dY} & v_0 \\ 0 & 0 & 1 \end{bmatrix} \begin{bmatrix} X \\ Y \\ l \end{bmatrix}$$

Furthermore, from the representation of world coordinate system $(O_w X_w Y_w Z_w)$ in the camera coordinate system $(Oxyz)$, the relationship between the world coordinate system (x_w, y_w, z_w) and the camera coordinate system (x, y, z) is obtained:

$$\begin{bmatrix} x \\ y \\ z \\ 1 \end{bmatrix} = \begin{bmatrix} n_x & o_x & a_x & p_x \\ n_y & o_y & a_y & p_y \\ n_z & o_z & a_z & p_z \\ 0 & 0 & 0 & 0 \end{bmatrix} \begin{bmatrix} x_W \\ y_W \\ z_W \\ 1 \end{bmatrix} = M_w \begin{bmatrix} x_W \\ y_W \\ z_W \\ 1 \end{bmatrix}$$

In the equation above, M_w is the external parameter matrix of camera; $[n_x, n_y, n_z]^T$ is the direction vector of X_W in $Oxyz$; $[o_x, o_y, o_z]^T$ is the direction vector of Y_W in $Oxyz$; $[a_x, a_y, a_z]^T$ is the direction vector of Z_W in $Oxyz$; $[p_x, p_y, p_z]^T$ is the offset vector of O_W in $Oxyz$.

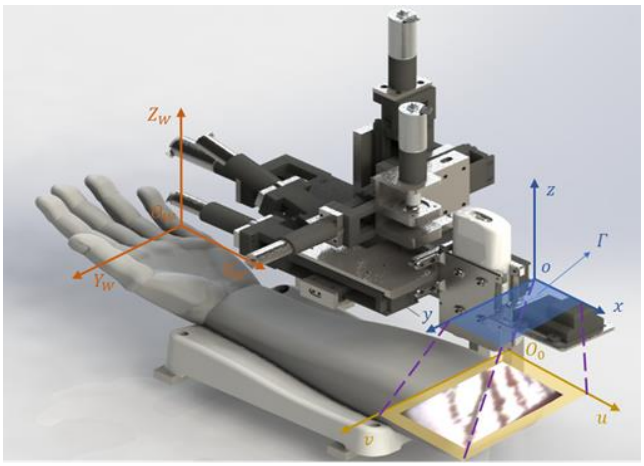

(a)

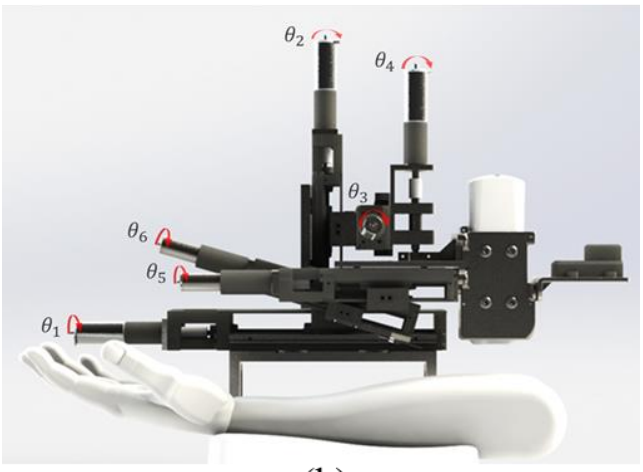

(b)

Fig. 6. (a) Coordinate Transformation of the Venipuncture Robot: the numbers; (b) The Angle position of the robot's motor.

Motor Control System

As depicted in Fig. 7, the motor control scheme is as follows. First, the 3-D coordinates of the selected target vein center are outputted from the NIR and the US vein segmentation algorithm and inputted into the inverse kinematic equations. Here, the joint parameters needed to position the needle at the desired location before the cannulation are calculated. The manipulator can dynamically steer the needle in real-time by tracking the injection site and vein walls in the US image to account for patient arm movement, tissue deformation, and vein rolling.

Our proposed deep learning network, allows us to continuously feedback on the updated desired injection site extracted from the US image. In this fashion, the US serves as image feedback to guide the needle manipulator in a closed-form control loop. Here, the cannula is steered into the vein until the needle tip reaches the center. By tracking the target vessel in real-time throughout the insertion, the device can compensate for rolling veins, tissue motion, and the viscoelastic nature of human tissue.

For motor control in the 3-DOF Needle Module, independent Digital Position Controllers (EPOS2, Maxon

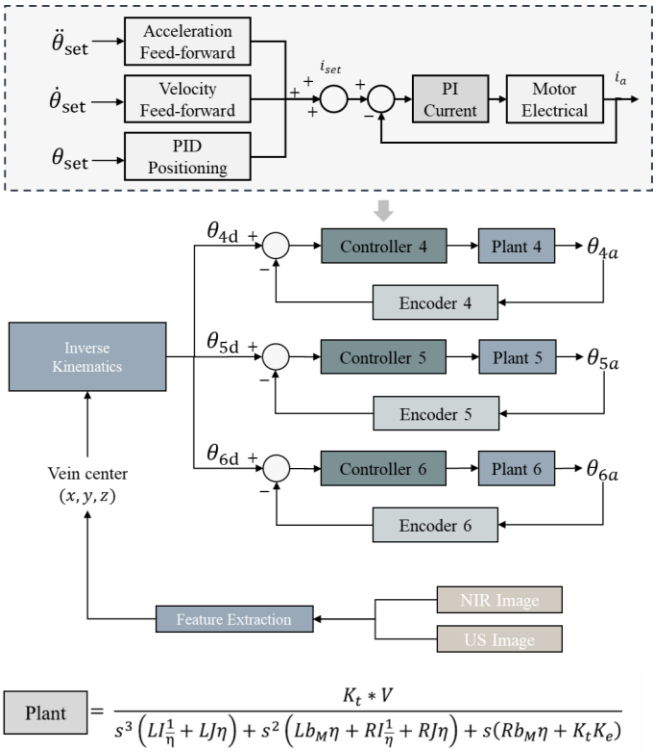

$$\text{Plant} = \frac{K_t * V}{s^3\left(LI_{\eta}^{1} + LJ\eta\right) + s^2\left(Lb_M\eta + RI_{\eta}^{1} + RJ\eta\right) + s(Rb_M\eta + K_tK_e)}$$

Fig. 7. Motor position feedback control and the target injection site is updated from the US at 20 Hz. Plants 1–3 have different rotational inertias.

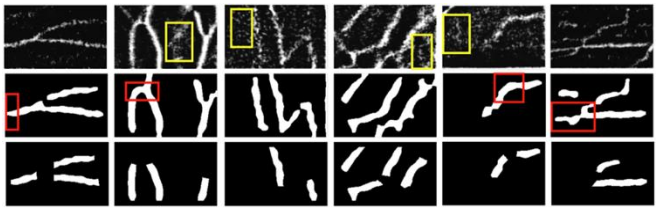

Fig. 8. Six examples of vein segmentation and suitable puncture areas: (top) original image; (middle) vein segmentation ground truth (GT); (bottom) suitable puncture area ground truth (GT). Red boxes illustrate the unsuitable puncture areas while yellow boxes illustrate the noises.

Motors) for each joint were utilized, which contain both motor drivers and encoder counters on the same board. We operated them using a controller area network protocol to send 32-bit PWM signals (100-kHz switching frequency) to the motors.

Medical Image Segmentation

Near-infrared

We randomly select six NIR images as examples and show the vein segmentation and suitable puncture areas in Fig. 8. We propose a Dual-In-Dual-Out network with two-step learning and two-task learning to determine the suitable puncture area and angle from the NIR image inputs. A visual illustration of the proposed network is shown in Fig. 9. It contains two steps of training: first, it trains a Single-In-Single-Out network to segment the vein from the NIR image; second, it inputs both the NIR image and vein segmentation from the first step training into the Dual-In-Dual-Out network to regress the suitable puncture area and angle.

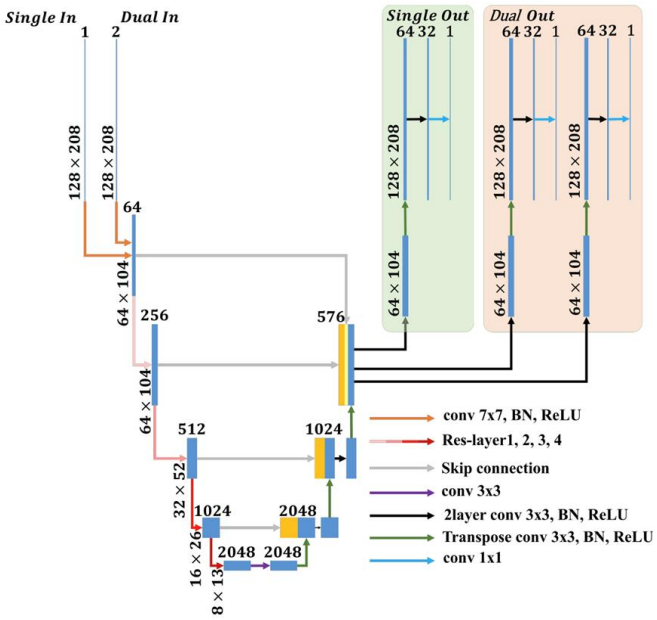

Fig. 9. An illustration of the Dual-In-Dual-Out ResNeXt50-Unet network structure.

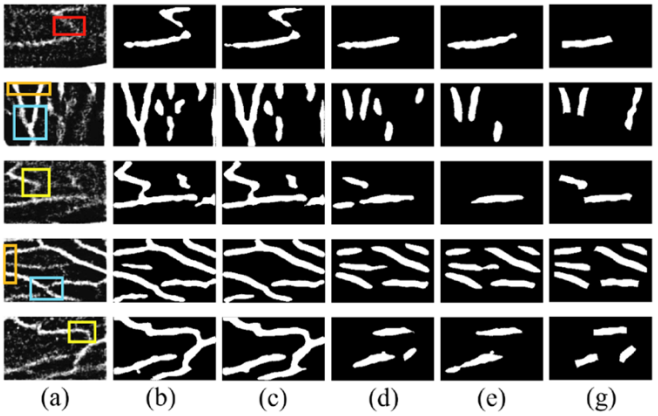

Fig. 10. An illustration of five suitable puncture area regression results: (a) original image; (b/c/d/e) suitable puncture area regression results of Single-In-Single-Out/Single-In-Dual-Out/Dual-In-Single-Out/Dual-In-Dual-Out network; (g) suitable puncture area GT. The red, orange, blue, and yellow box indicates non-suitable puncture areas, including the short vein, vein closed to the imaging edge of NIR camera, vein bifurcation and largely curved vein respectively.

Five examples of the suitable puncture area regression by the four methods are shown in Fig. 10. We can visually see that both the Dual-In-Single-Out and Dual-In-Dual-Out network can distinguish between the suitable and non-suitable puncture area better than the Single-In-Single-Out and Single-In-Dual-Out network, indicating the importance and value of bringing the vein segmentation into the network's input. For the regression of suitable puncture areas and angle, The mean and std DSC are shown in Table I and Table II.

Ultrasonic

An illustration of the dataset is shown in Fig. 11, where green boxes illustrate the veins, yellow boxes illustrate the vein shadow and red boxes represent the vessel edges. In previous studies, UNet, FPN, and other models have shown

TABLE I: The mean and std DSC (in percentage) of vein segmentation achieved by Single-In-Single-Out network, and that of suitable puncture area regression achieved by Single-In-Single-Out, Single-In-Dual-Out, Dual-In-Single-Out, and Dual-In-Dual-Out network.

Task	Method	Fold 0	Fold 1	Fold 2	Fold 3	Fold 4	Average
Vein segmentation	Single-In-Single-Out	77.34±10.56	76.93±12.47	73.19±10.17	79.26±6.99	76.76±8.36	76.70±10.09
Puncture regression	Single-In-Single-Out	53.15±19.92	57.16±16.91	56.23±16.47	55.13±19.07	57.49±16.50	55.83±17.90
	Single-In-Dual-Out	54.77±19.73	54.85±18.11	56.67±16.95	56.66±18.93	57.39±17.78	56.80±18.36
	Dual-In-Single-Out	72.76±15.62	**75.76±17.65**	74.15±13.36	**77.02±18.90**	**76.79±14.67**	75.53±16.24
	Dual-In-Dual-Out	**75.50±14.53**	75.30±17.87	**78.00±13.85**	74.15±13.36	76.19±19.72	**76.34±16.69**

TABLE II: The mean and std DSC (in percentage) of vein segmentation achieved by Single-In-Single-Out network, and that of suitable puncture area regression achieved by Single-In-Single-Out, Single-In-Dual-Out, Dual-In-Single-Out, and Dual-In-Dual-Out network.

Task	Method	Fold 0	Fold 1	Fold 2	Fold 3	Fold 4	Average
Angle regression	Single-In-Single-Out	-	-	-	-	-	-
	Single-In-Dual-Out	20.07±16.91	25.32±20.13	25.25±21.61	23.08±20.02	23.89±18.86	23.57±19.68
	Dual-In-Single-Out	14.62±14.78	18.31±14.23	**21.19±17.70**	13.57±15.22	17.93±16.72	17.28±16.06
	Dual-In-Dual-Out	**14.35±15.82**	**13.21±14.76**	21.57±19.47	**13.29±16.42**	**14.90±13.75**	**15.58±16.47**

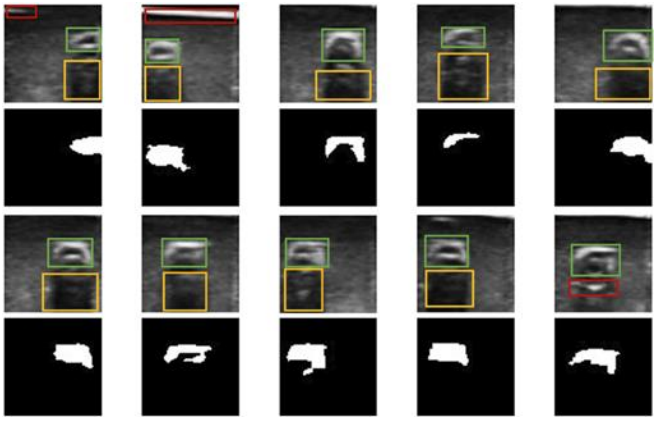

Fig. 11. Eight examples of ultrasonic angiography (top) with their corresponding ground truth (GT) labelled pictures of best puncture area (bottom): green boxes illustrate the veins; yellow boxes illustrate the vein shadows; red boxes illustrate the vessel edges; binary graphs illustrate the vein region.

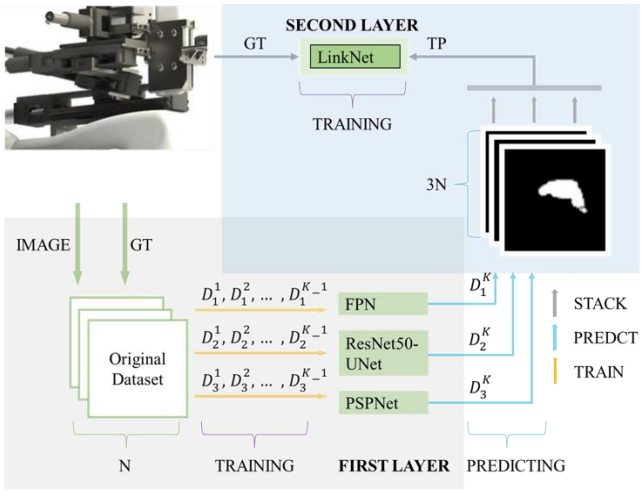

Fig. 12. The General Structure of ISM

good performance in image segmentation. To merge the advantages of these deep-learning neural networks, our model integrates multiple image segmentation networks. Through stacking methods and feature image coding, we propose the Integrated Segmentation Model (ISM), offering high precision for vein segmentation from ultrasonic images. As shown in Fig. 12, the overall structure of ISM includes two layers. The first layer is composed of three sub-models (FPN, PSPNet, and UNet, numbered as models 1, 2, and 3). The output result diagram of the first layer was used as the input training picture of the second layer. The second layer of the sub-model is composed of LinkNet, which takes the label picture (GT) of the original data set as the recognition target.

As can be seen in Table II, the proposed ISM demonstrates its superiority over traditional models in terms of the three indicators, namely Dice-Similarity-Coefficient (DSC), Hausdorff-Distance (HD95) and Intersection-Over-Union (IOU). The ISM model achieved significant improvements in multiple indicators: its DSC value increased by about 6 %, reaching 94.62 %, and the IOU value increased by about 11%, in complex samples. Finally, a clear puncture point is calculated through the connection domain algorithm. Experimentally, the success rate of selecting the suitable vein for puncture is 99.21%.

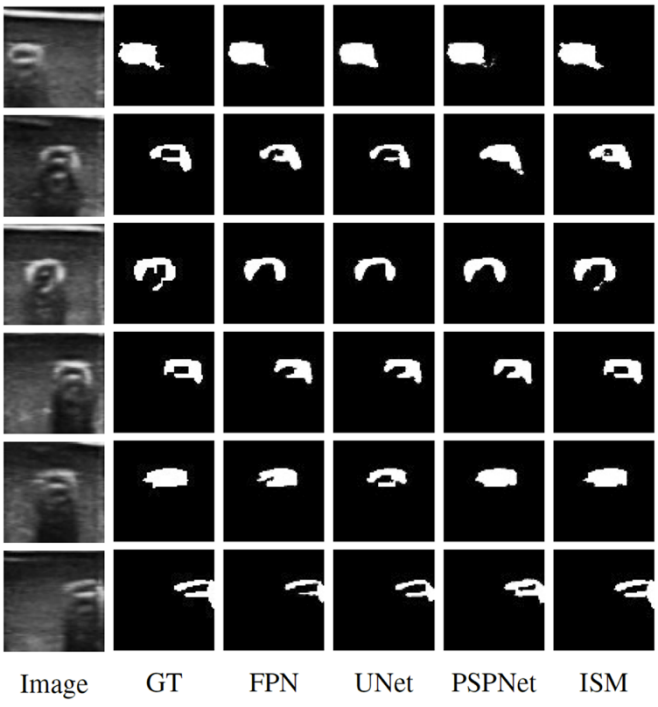

Fig. 13. Vein segmentation results of different models: FPN, Unet, PSPNet, ISM; GT illustrates the label picture for the dataset.

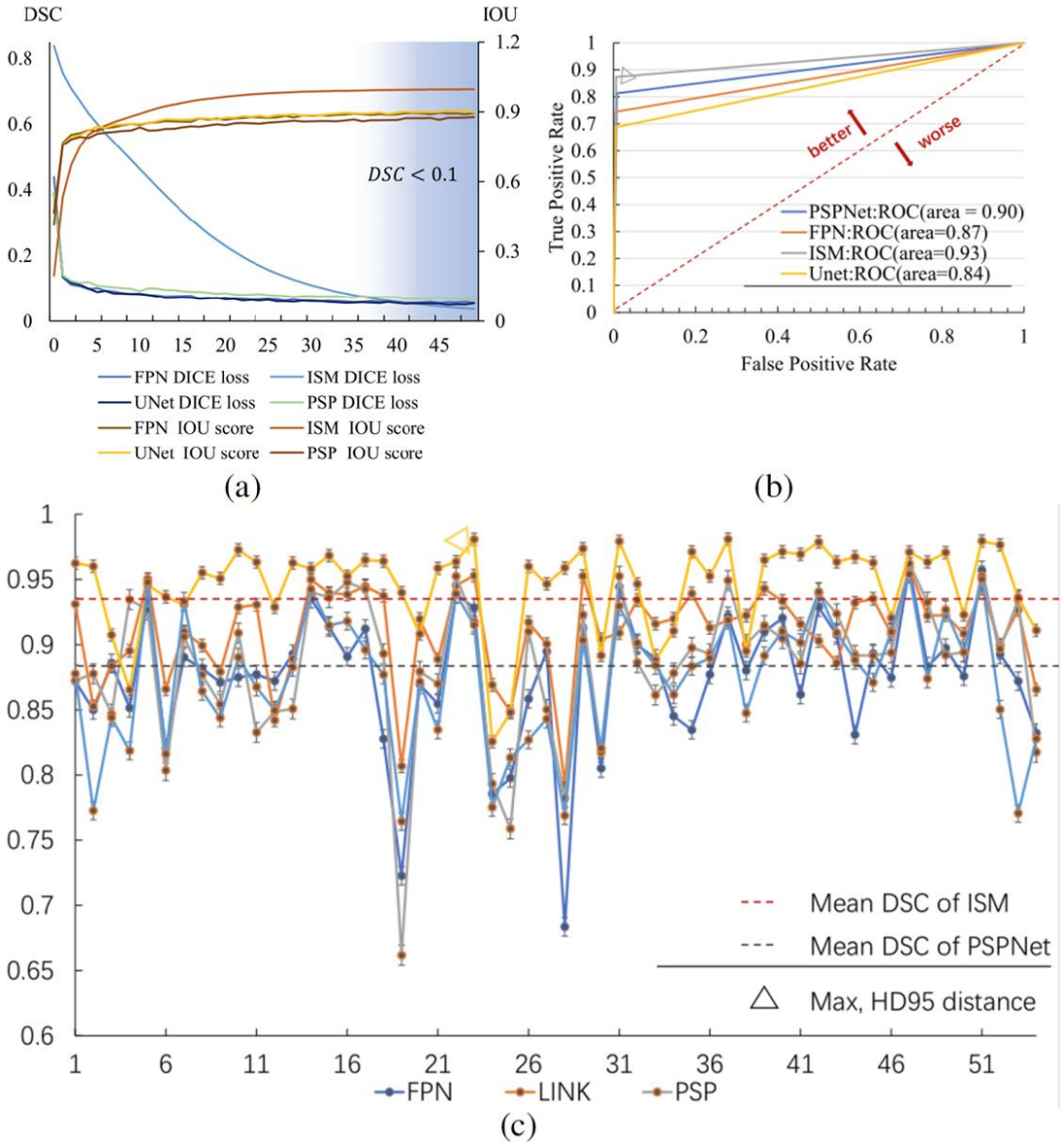

Fig. 14. Training procedure of the FPN, UNet, PSPNet and ISM: (a) Dice Loss curve of FPN, UNet, PSPNet, ISM. (b) ROC-AUC curve of FPN, UNet, PSPNet, ISM of testing picture. (c) The DSC curve of vein segmentation results using different models: FPN, UNet, PSPNet, LinkNet, ISM.

TABLE III: DSC and HD95 metrics of the proposed ISM model and others traditional segmentation models

	DSC			HD95			IOU		
	Mean	Max	Min	Mean	Max	Min	Mean	Max	Min
FPN	0.873535	0.959378	0.683639	7.630993	15.0	3.605551	0.826387578	0.942417796	0.604443894
UNet	0.871502	0.953982	0.652896	7.758953	15.0	5.0	0.828625436	0.949215443	0.557574728
PSPNet	0.881807	0.962169	0.661774	7.650129	15.0	5.0	0.826387578	0.942417796	0.604443894
ISM	**0.946176**	**0.983374**	**0.822243**	**6.901212**	**11.18034**	**4.123106**	**0.93446422**	**0.98640774**	**0.751974682**

TABLE IV: Actual veinpuncture results of different models.

	Model Identification Error(mm)			Puncture Error(mm)			Failure Rate of Vein Selection(%)		
	model 1	model 2	model 3	model 1	model 2	model 3	model 1	model 2	model 3
FPN	7.23	4.22	7.14	8.83	5.89	9.35	6.36	4.42	5.8
UNet	6.13	6.24	9.13	8.19	9.89	11.13	5.72	6.92	3.24
PSPNet	6.13	5.14	3.12	7.54	6.35	4.21	9.24	8.47	5.89
ISM	**0.13**	**0.21**	**0.86**	**1.65**	**1.32**	**1.13**	**0.78**	**0.17**	**0.50**

Ergonomic Design

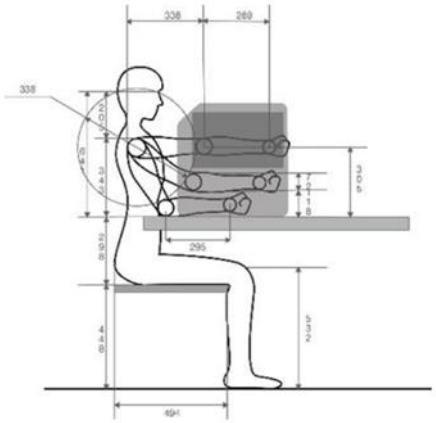

Fig. 15. Design dimensions and usage scenarios

To make the robot more reasonable, we adopt the most relaxed lancing posture of human limbs (adult standard) through ergonomic measurement and calculation(Fig. 15).

The portable Venipuncture Robot we invented has a size of 0.376*0.253*0.298 m^3, which greatly reduces the volume compared with similar robots in 1*1*1.5 m^3. At the same time, using POM mixed materials, the mass of our robot is in the range of 6kg, about 15% of similar robots, making it more portable.

Puncture Experiment

To validate the assembly accuracy and stability of the automatic venipuncture robot, we carried out experiments multiple times to test its positioning error. Different sizes of circles on the printed paper were used to simulate blood vessels of different sizes (with diameters ranging from 3-5mm). The center of the circle was set as the puncture target point, and the distance from the center of the puncture point was taken as the measurement standard of puncture accuracy. We use a marker instead of a needle to mark puncture points on paper. The simulated puncture results are shown in Fig. 16 (a) (marked points in the red circle). After 10 groups of tests, we collected and analyzed the data, the result is shown in Fig. 16 (b).

It was determined that the maximum puncture error of the puncture robot was 1.79mm and the minimum error was 0.91mm. At the same time, according to the principle that if the final point's position drawn by the pencil falls within the radius, it is recognized as a successful puncture, otherwise, it fails, the success rate of the test was 98.24%.

Application and Prospect

Through mathematical modeling and the puncture experiments, the venipuncture robot can effectively relieve the working pressure of medical staff, and at the same time, reduce the risk of cross-infection among medical staff in the context of the COVID-19 pandemic.

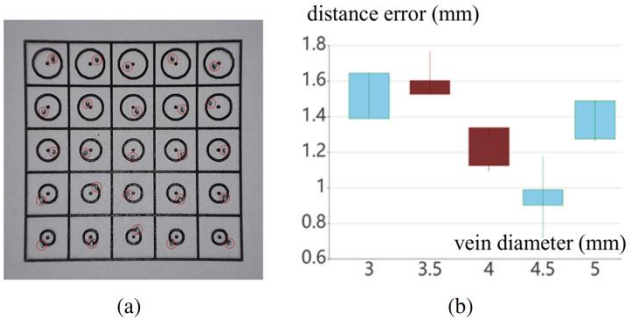

Fig. 16. Evaluation of positioning error of the robot: (a) testing paper with simulated blood vessel (diameter: 3mm-5mm) and the simulated puncture point marked with red circles (b) positioning error distribution diagram under different blood vessel diameters (3mm-5mm).

Fig. 17. A team of doctors, nurses and physiotherapists take care of critical patients with COVID-19 in the ICU of the Vila Nova Cachoeirinha hospital, north of São Paulo.

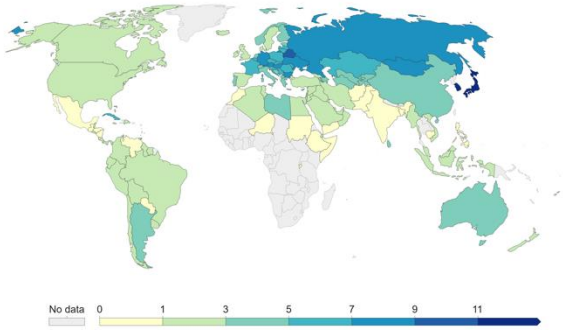

Fig. 18. Hospital beds per 1000 people in 2020

Of course, it is more valuable for the specific populations, such as elder people, infants, or people with shock state. For instance, some elderly patients need long-term puncture, thus may causing hematoma, phlebitis, artery or nerve damage due to repeated puncture, and the robot can find more puncture sites and perform more precise puncture, which can effectively reduce the pain of patients.

The robot can not only walk into the hospital, the community, but also walk into the home, applied in the laboratory. Because of its high degree of automation, simple and easy to operate, operators do not need professional medical knowledge, it can be convenient to provide puncture services. At the same time, it has obvious advantages in

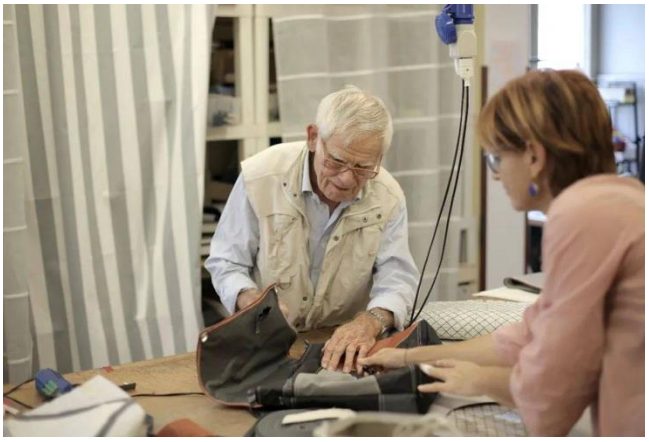

Fig. 19. The clinic staff are attending to the old man

Fig. 20. Mice were subjected to general anesthesia by intraperitoneal injection in the laboratory.

Fig. 19. A nurse prepares to take a blood sample from a vein in a little girl's arm.

controlling variables, improving efficiency, which can accelerate the experimental progress.

Acknowledgement

We would like to thank the medical staff and the workshop workers for their hard work and suggestions. Research reported in this publication was supported by the Innovation and Entrepreneurship Program. Meanwhile, we acknowledge additional support from School of Electronic and Information Engineering, College of Mechanical Engineering and the hospitals that we cooperate with.